atmosphere

MDPI

Article

Deployment and Performance of an X-Band Dual-Polarization Radar during the Southern China Monsoon Rainfall Experiment

Zhao Shi [1,2,3], Haonan Chen [4], Venkatachalam Chandrasekar [4] and Jianxin He [3,*]

1 Institute of Mountain Hazards and Environment, Chinese Academy of Sciences, Chengdu 610041, China; shi_zhao@foxmail.com
2 University of Chinese Academy of Sciences, Beijing 100049, China
3 Key Laboratory of Atmospheric Sounding, Chengdu University of Information and Technology, Chengdu 610225, China
4 1373 Campus Delivery, Colorado State University, Fort Collins, CO 80523, USA; haonan.chen@colostate.edu (H.C.); chandra@colostate.edu (V.C.)
* Correspondence: hjx@cuit.edu.cn; Tel.: +86-028-8596-7291

Received: 25 October 2017; Accepted: 24 December 2017; Published: 26 December 2017

Abstract: An X-band dual-polarization radar (XPRAD) was deployed in Guangdong province as part of the Southern China Monsoon Rainfall Experiment (SCMREX) during the storm season in 2016. This paper presents a comprehensive assessment of XPRAD observations during SCMREX with emphasis on data processing and rainfall products. The differential phase-based attenuation correction and radar calibration using self-consistency of dual-polarization observables are presented. It is found that the standard deviation of the Z_{dr} bias is less than 0.2 dB based on 'light rain at low angle' and 'dry aggregate snow' observations. Cross-comparison with two standard S-band China New Generation Weather Radars (CINRAD) shows that the bias of Z_h has a mean value less than 1.5 dBZ and a standard deviation less than 0.5 dBZ. In addition, fifteen rainfall events that occurred during the intensive observing period (IOP) are analyzed to demonstrate the rainfall estimation performance of XPRAD. In particular, rainfall accumulations at 1-, 2- and 3-h scales derived using $R(K_{dp})$ and $R(Z_h, Z_{dr})$ relations are evaluated using national level rain gauge data and CINRAD-based rainfall estimation. The results show that both $R(K_{dp})$- and $R(Z_h, Z_{dr})$-based products agree well with the rain gauge observations and CINRAD estimation. The difference between $R(K_{dp})$ and $R(Z_h, Z_{dr})$ is not significant, although $R(K_{dp})$ shows slightly better performance than $R(Z_h, Z_{dr})$.

Keywords: dual-polarization; X-band; radar; QPE; SCMREX

1. Introduction

Heavy rainfall annually occurs from mid-April to mid-June in southern China, often inducing flooding and geological disasters, causing devastating property damage and loss of life. Precipitation over this period, well-known as the southern China monsoon rainfall, accounts for nearly half of the total annual precipitation. However, quantitative precipitation estimation and forecasting (QPE/QPF) in this region remains a challenge since the monsoon mechanism is not yet well understood due to the complicated multiscale atmospheric processes involved [1]. In 2016, the Southern China Monsoon Rainfall Experiment (SCMREX) was conducted in order to further understand the physical mechanism of monsoon rainfall in the pre-summer season and improve the performance of QPE [1]. Weather radar was a key component of providing accurate quantitative precipitation estimations during the setup of SCMREX. Currently, there are 14 operational S-band China New Generation Weather Radars (CINRAD) in Guangdong province, providing routine weather observations for the whole province.

However, the CINRAD radars operate through pre-defined scan strategies, which have a slow update rate of five–six min and cannot be changed. In addition, these S-band radars operate at long ranges (i.e., 460 km maximum), resulting in most of the lower atmosphere not being able to be observed due to the Earth's curvature. On the other hand, the application of short range X-band radars is gaining more interest worldwide in recent years. X-band radar has some evident advantages, including higher mobility, smaller size, lower cost and power consumption, potentially higher spatial resolution and stronger differential phase signals. Some typical applications of X-band radar include: the X-band radar network for Collaborative Adaptive Sensing of the Atmosphere (CASA) [2–4], the X-band radar of NOAA/Environmental Technology Lab (ETL) for Hydro-meteorological Testbed (HMT-04) project [5], the mobile X-band dual-polarization radar (XPOL) of National Observatory of Athens for the International H_2O Project (IHOP) [6], the X-band polarimetric radar network (X-NET) in the Tokyo metropolitan area of Japan [7], and the X-band dual-polarization radar of the Korea Institute of Civil Engineering and Building Technology (KICT) for the urban rainfall observation [8]. To this end, an X-band dual-polarization weather radar (XPRAD) was deployed in Xinfeng County (Shaoguan, China) to play a gap-filling role, and it is the first X-band polarization radar for the SCMREX field campaign. The XPRAD radar has the capability of providing high-resolution rainfall observations within the CINRAD operational radar coverage. The adaptive scanning strategy of the XPRAD radar also increases its operability to fast-moving mesoscale convective systems.

However, reflectivity (Z_h) and differential reflectivity (Z_{dr}) measured by X-band radar are attenuated by heavy rain and supposed to be limited for heavy rainfall observations. Z_h and Z_{dr} should be corrected for attenuation before use for quantitative applications such as QPE. Although there is no standard algorithm to adopt for attenuation correction, the differential propagation phase (Φ_{dp}) based approach has been fairly successful in recent years. Testud et al. [9] proposed a method termed as 'ZPHI' to correct rainfall reflectivity profile with Φ_{dp} constraint for space-borne radar. Matrosov et al. [10] calculated the total attenuation for Z_h and Z_{dr} with a fixed linear dependence on Φ_{dp}. In addition, the specific differential phase (K_{dp}) based rainfall relations are commonly used at higher frequencies such as the X and Ku band [11], since they are insensitive to radar calibration, partial beam blockage, rainfall attenuation, and hail contamination, moreover, K_{dp} has an approximate linear relation with rainfall rate. The self-consistency of dual-polarization observations also shows that K_{dp} can be used to estimate the specific attenuation at horizontal polarization (A_h) and specific differential attenuation (A_{dp}) [12,13]. Gorgucci et al. [14] present a self-consistent iterative scheme which can be directly applied to an entire radar ray. In order to improve the accuracy of the A_h and A_{dp} parameterized from dual-polarization measurements, Kalogiros et al. [15] enhanced the self-consistent iterative scheme using parameterization functions with a minimum parameterization error of A_h and A_{dp}. This article utilizes the drop size distribution (DSD) data captured during SCMREX to derive the polarimetric observables with the T-matrix method at the X-band frequency [16], and regresses the nonlinear relationship of $A_h - K_{dp}$ and $A_{dp} - A_h$.

Before applying any rainfall estimate algorithm, system bias errors in Z_h and Z_{dr} must be evaluated. System biases in Z_h and Z_{dr} are often caused by the difficulty of precisely calibrating the radar hardware and its time variability during operation. The accuracy of 1 dB and 0.2 dB for Z_h and Z_{dr} are required, respectively [17]. There are several methods to identify the bias of Z_{dr} and Z_h. The Z_{dr} of raindrops with a diameter size less than 0.5 mm is ideally equal to zero dB, due to the spherical shape of tiny drops, which can be applied to regular volume radar data from a low elevation angle [18] (hereafter referred to as the 'light rain at low angle' approach). The Z_{dr} of dry aggregated snow above the melting layer is less than 0.2 dB at the 60° elevation, which can be used as the expected value for calibrating [17] (hereafter referred to as the 'dry aggregated snow' approach). Kalogiros et al. [15] determined Z_h bias through comparison with X-band reflectivity values calculated from comparison with the disdrometer data at low rain-path attenuation. The systematic bias of Z_h also can be evaluated based on the self-consistency principle [19]. It is demonstrated that the rainfall estimated by Z_h and Z_{dr} should be the same as that estimated by the unbiased variable of K_{dp}

when measurements are not affected by bias [20]. The bias in the Z_h can be confirmed by comparing the reconstructed K_{dpc} from Z_h and Z_{dr} with the radar estimated K_{dp} [18]. This study applies the self-consistency principle to correcting the system errors of Z_h, upon the completion of attenuation correction and Z_{dr} systematic bias correction.

In order to evaluate the observation and performance of the XPRAD radar, scross-validations with S-band radars and rain gauges are performed. There are two S-band radars near the XPRAD radar. This is performed to compare reflectivity from the common radial coverage between the XPRAD and S-band radar to verify the composite effectivity of attenuation correction and bias assessment. Cross-validation with rain gauge observations and S-band radar rainfall estimation aims to assess the performance of the XPRAD-based QPE. Therefore, the $R(K_{dp})$ and $R(Z_h, Z_{dr})$ as the relationships between the rainfall rate and polarized variables are used to estimate rainfall accumulation and compare with rain gauge observations and S-band radar rainfall estimation.

The paper is organized as follows. In Section 2, an overview of the XPRAD radar system and observations during SCMREX is provided. Validation of the attenuation correction and systematic bias assessment are discussed in Section 3. Performance evaluations of the rainfall estimate are presented in Section 4. The main findings of this paper are summarized in Section 5.

2. System Description and Deployment during SCMREX

The field campaign of SCMREX aims to capture composite high spatiotemporal resolution observations to detect the atmospheric environment and internal fine structures of the storm during the pre-summer rainy season in southern China. As a part of the whole composite observing network, the XPRAD radar is deployed in Xinfeng County and mainly observes the atmospheric evolution at the south of the radar where heavy rain belts occur during the pre-summer season. There are two S-band radars near the XPRAD radar, one is located in Guangzhou City (Site No. 9200), and the other is located in Heyuan City (Site No. 9672). In order to obtain the rainfall rate retrieval algorithms for XPRAD, one autonomous parsivel (particle size and velocity) unit (APU) was deployed at the Longmen national meteorological station and DSD measurements from the APU were used to simulate the rainfall rate and dual-polarization radar measurements. Within the 80 km detection range of XPRAD, there are six national-level meteorological stations where the rain gauges are well-maintained and provide ground validation of radar-based rainfall estimates.

Figure 1 shows the layout of the XPRAD radar, the S-band radars, APU and rain gauges. Table 1 shows the performance specifications for the XPRAD radar.

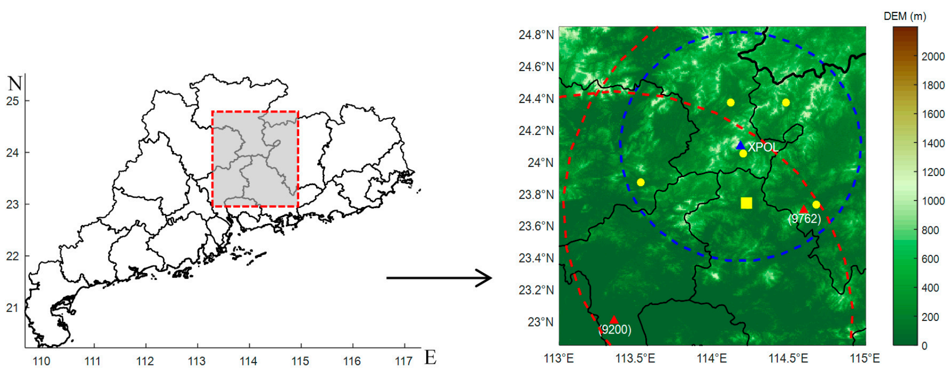

Figure 1. Layout of the X-band dual-polarization radar (XPRAD), two S-band radars and national meteorological station. The blue triangle represents the location of XPRAD, blue dash circle line indicates that the detection range of XPRAD is 80 km. The red triangle represents the locations of two S-band Doppler radars (9200 and 9762), red dash circle line indicates that the detection range of the two radars is 150 km. The yellow circle dot indicates the rain gauges which are deployed at the national meteorological station. The yellow square represents the location of one autonomous parsivel unit (APU) and one rain gauge which are deployed at the Longmen national meteorological station.

Table 1. System characteristics of the XPRAD radar.

Item	Value
Wavelength	X
Antenna Diameter/m	2.4
Antenna Gain/dBi	44
3 dB Beam width/°	0.95
Polarized mode	Simultaneous Horizontal and Vertical Polarization (SHV)
Transmitted Peak Power/W	200
Bandwidth/mHz	2
Noise Figure/dB	4
Dynamic Range/dB	95
Base Data	Z_h, V, W, Z_{dr}, ρ_{hv}, Φ_{dp}
Altitude above sea level	874 m

The intensive observation period (IOP) of the XPRAD radar lasted from 15 May to 15 June in 2016; the radar observations for fifteen rainfall events during IOP were captured. Detailed information about the rain events can be found in Table 2.

Table 2. Rainfall events list observed by XPRAD during intensive observation period (IOP) in pre-summer season.

No.	Date	Duration Time (BJT, UTC + 8:00)	Rainfall Basic Characteristic	Evolving Direction	
				From	To
1	20 May 2016	00:00–24:00	Stratiform	Southwest	Northeast
2	21 May 2016	00:00–13:00	Convective	Southwest	Northeast
3	28 May 2016	00:00–24:00	stratiform	South	North
4	29 May 2016	00:00–24:00	Convective	Southwest	Northeast
5	03 June 2016	10:30–24:00	stratiform	West	East
6	04 June 2016	00:00–24:00	stratiform	West	East
7	05 June 2016	03:00–12:21	Convective	West	East
8	08 June 2016	02:00–15:50	Convective	Southwest	Northeast
9	09 June 2016	12:57–24:00	Convective	South	North
10	10 June 2016	00:00–10:30	Convective	South	North
11	11 June 2016	02:00–24:00	Convective	Southwest	Northeast
12	12 June 2016	00:00–24:00	Convective	Northwest	Southeast
13	13 June 2016	00:00–24:00	Stratiform	West	East
14	14 June 2016	00:00–24:00	Convective	West	East
15	16 June 2016	01:30–14:30	stratiform	Southwest	Northeast

3. Attenuation Correction and Bias Assessment

3.1. Raindrop Model and Polarimetric Radar Observables Simulation

The performance of XPRAD was evaluated with three parts as: attenuation, systematic bias and rainfall estimation. The main procedure was performed as shown in the Figure 2. The self-consistency approach for attenuation correction and bias assessment requires several empirical relationships related to polarization variables, such as: $A_h\left(K_{dp}\right)$, $A_{dp}(A_h)$, and $K_{dp}(Z_h, Z_{dr})$, and these relationships are sensitive to changes in DSD, drop shape and temperature, etc. Rainfall estimators including $R\left(K_{dp}\right)$, $R(Z_h)$, and $R(Z_h, Z_{dr})$ were also simulated and used to evaluate the QPE performance. Therefore, radar observables and some factors determining the derivation of those relations are briefly described here.

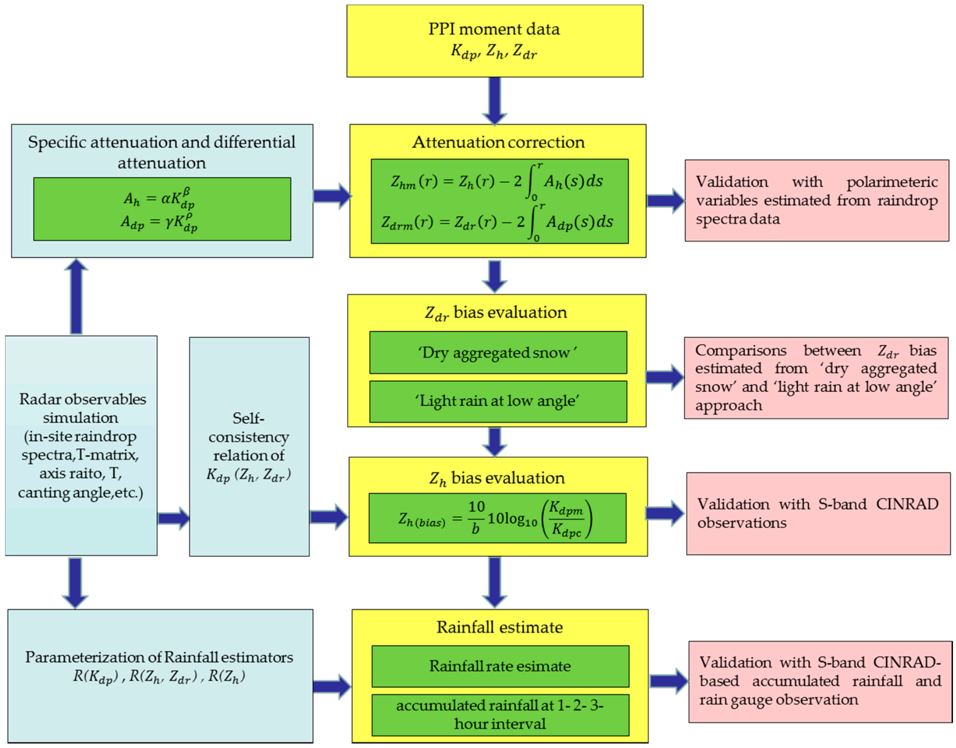

Figure 2. Flow diagram describing the procedure to evaluate the performance of XPRAD.

Microphysical property of rain medium can be represented by the drop size distribution. A good knowledge of DSD is a prerequisite for deriving radar observables, specific attenuation and rainfall algorithms. In general, a water-content-normalized gamma DSD model can adequately account for the natural variations in the shape of rainfall DSD [9,19]:

$$N(D) = N_w f(\mu)\left(\frac{D}{D_0}\right)^{\mu} \exp\left[-(3.67+\mu)\frac{D}{D_0}\right] \tag{1}$$

$$f(\mu) = \frac{6}{(3.67)^4}\frac{(3.67+\mu)^{\mu+4}}{\Gamma(\mu+4)} \tag{2}$$

where $N(D)$ is the number of raindrops per unit volume per unit size interval, D is the volume equivalent spherical diameter in the unit of mm, D_0 is the median volume diameter, μ is a distribution shape parameter, and N_w is the normalized intercept parameter of an equivalent exponential distribution with the same water content and D_0. In this study, DSD measured by APU are used to derive the relations among the polarimetric variables. The raindrop spectra were collected every minute during the IOP and quality control procedures were first applied to check the raindrop spectra before simulation, as follows: raindrop spectra were discarded if the number of channels with nonzero counts was less than six, the rainfall rates observed by APU were less than 0.1 mm/h. In addition, raindrop spectra were integrated over 3 min intervals to represent the average status of the radar's sampling volume [6]. A total of 5880 raindrop spectra were valid for rainfall events and then used to estimate the parameters of a normalized gamma DSD model.

The rain drop shape model (axis ratios) used in the study is a composite relation of the Andsager et al. fit for 0.11 cm $\leq D \leq$ 0.44 cm [21], and the Beard and Chuang model for $D <$ 0.11 cm, $D >$ 0.44 cm [22], defined as:

$$a/b = \begin{cases} 1.0048 + 0.0057D - 2.628D^2 + 3.682D^2 - 1.677D^4 & D < 0.11\ \text{cm},\ D > 0.44\ \text{cm} \\ 1.012 - 0.144D - 1.03D^2 & 0.11\ \text{cm} \leq D \leq 0.44\ \text{cm} \end{cases} \tag{3}$$

form of DSD. Specific differential phase K_{dp} can be expressed as:

$$K_{dp} = \frac{180\lambda}{\pi} \mathrm{Re} \int [f_h(D) - f_v(D)] N(D) dD \tag{4}$$

where λ is the radar wavelength; f_h and f_v are the complex forward-scatter amplitudes at horizontal and vertical polarizations, respectively. The two-way differential propagation phase Φ_{dp} is described as:

$$\Phi_{dp} = 2 \int K_{dp}(r)\, dr \tag{5}$$

The measured differential propagation phase is expressed as:

$$\Psi_{dp} = \Phi_{dp} + \delta_{hv} \tag{6}$$

where Ψ_{dp} is the total differential phase and can be estimated from copolar covariance, δ_{hv} is the backscattering propagation phase.

The reflectivity factors $Z_{h,v}$ at horizontal and vertical polarizations are defined as:

$$Z_{h,v}\ (\mathrm{dBz}) = 10 \log_{10} \left[\frac{\lambda^4}{\pi^5 |K_w|^2} \int \sigma_{h,v}(D) N(D) dD \right] \tag{7}$$

where σ_h and σ_v are the radar cross-section at horizontal and vertical polarization, respectively; K_w is the dielectric factor of water given by $K_w = (\varepsilon_r - 1)/(\varepsilon_r + 2)$, here ε_r is the complex dielectric constant of water. Differential reflectivity Z_{dr} is defined as the ratio of reflectivity factor at horizontal and vertical polarizations:

$$Z_{dr}\ (\mathrm{dB}) = 10 \log_{10} \left[\frac{\int \sigma_h(D) N(D) dD}{\int \sigma_v(D) N(D) dD} \right] \tag{8}$$

Specific attenuation at the horizontal and vertical polarization and differential attenuation are defined in the integral form of DSD as

$$A_{h,v} = 4.343 \times 10^{-3} \mathrm{Im} \int f_{h,v}(D) N(D)\, dD \tag{9}$$

$$A_{dp} = A_h - A_v \tag{10}$$

where $A_{h,v}$ and A_{dp} in the unite of dB km^{-1}.

The scattering simulations for this study were performed with the T-matrix approach [23] and in-site raindrop spectra obtained from APU, and the following conditions were considered for simulations: the wavelength of XPRAD and CINRAD, average atmosphere temperature at 28 °C, the axis ratio model defined in Equation (3), a Gaussian canting angle distribution with zero mean and the standard deviation of 10° [24], an 8-mm maximum drop diameter.

3.2. Specific Differential Phase-Based Attenuation Correction

At X-band, the attenuation of signals due to scatter and absorption by the raindrops limits the accuracy of power measurements of radars. In rain, the amount of attenuation depends on the drop size distribution (DSD), the raindrop's extinction cross-section and atmosphere temperature. Due to its cumulative propagation effect, attenuation results in the fading of the reflectivity (Z_h) and differential reflectivity (Z_{dr}). Once A_h and A_{dp} are determined as a function of range, the attenuation correction of Z_h and Z_{dr} at a given range can be easily accomplished, respectively. The attenuated Z_{hm} and Z_{drm} are related to the corrected Z_h and Z_{dr}, defined as below:

$$Z_{hm}(r) = Z_h(r) - 2 \int_0^r A_h(s) ds \tag{11}$$

$$Z_{drm}(r) = Z_{dr}(r) - 2\int_{0}^{r} A_{dp}(s)ds \tag{12}$$

A_h and A_{dp} can be determined with an empirical relationship based on K_{dp} under scattering constraints, defined as:

$$A_h = aK_{dp}^{\beta} \tag{13}$$

$$A_{dp} = \gamma A_h^{\rho} \tag{14}$$

It is worthwhile noting that the exponent β and ρ are close to unity, and the linearity has a good approximation at frequencies from 2.8 to 9.3 GHz [25,26]. Due to the variation of raindrop shape, the coefficient α varies from 0.139 to 0.335 dB/deg and the coefficient γ also varies from 0.114 to 0.174 dB/deg. The variation differences of β or ρ influenced by temperature is much smaller than that of coefficient α or γ. The uncertainty of α and γ accounts for 28% or 17% relative errors to the mean value respectively [12]. The simulations for $A_h - K_{dp}$ and $A_{dp} - A_h$ were performed as shown in the scatterplot of Figure 3. Through nonlinear regression processing, α and γ here are 0.323 and 0.131, β and ρ are 1.05 and 1.2, as shown in Table 3. The correlation coefficient between A_h and K_{dp}, A_{dp} and A_h is 0.99 and 0.96, respectively, and indicates that the empirical relations are eligible for attenuation correction at the X band, based on the self-consistent method.

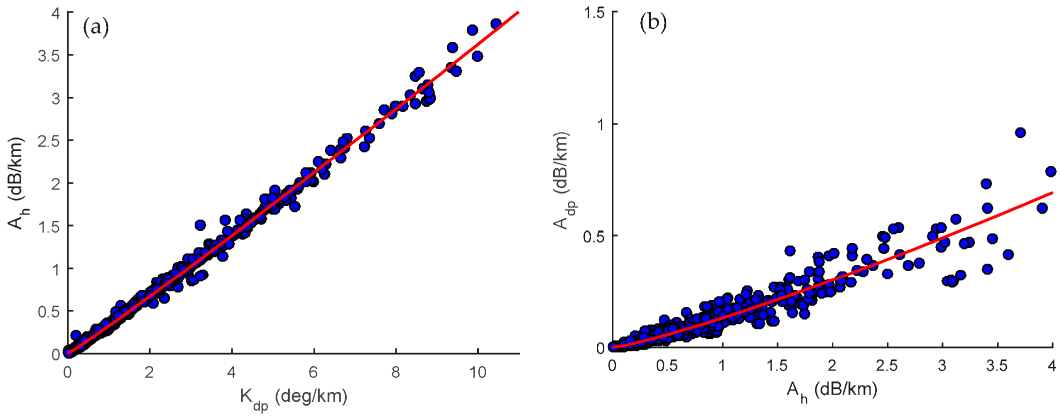

Figure 3. Scattergram of A_h, A_{dp} and K_{dp} derived from rain drop size distribution (DSD) data for fifteen rainfall events. The power law relations between attenuation and specific differential phase are derived: (**a**) $A_h = 0.323K_{dp}^{1.05}$; (**b**) $A_{dp} = 0.131A_h^{1.2}$.

Table 3. Coefficients for the relations of $A_h\left(K_{dp}\right)$, $A_{dp}(A_h)$, and $K_{dp}(Z_h, Z_{dr})$, at X-band. These polarimetric observables are simulated by T-matrix calculation.

$A_h = \alpha K_{dp}^{\beta}$		$A_{dp} = \gamma A_h^{\rho}$		$K_{dp} = aZ_h^b Z_{dr}^c$		
α	β	γ	ρ	a	b	c
0.323	1.05	0.131	1.2	2.22×10^{-4}	1	−4.58

In order to evaluate the attenuation correction performance, fifteen precipitation events during IOP were chosen to accomplish the K_{dp} retrieval and attenuation correction of Z_h and Z_{dr}. Figure 4 shows a storm example case occurred at 11:57 (BJT: time of Beijing, UTC + 8:00) on 5 June 2016, including corrected polarimetric variables observed by XPRAD and reflectivity observed by the two nearest S-band CINRAD (9200 and 9762). In the K_{dp} image (Figure 4b), a strong echo with a high K_{dp} above 3° km^{-1} occurred in the region marked with 'A' where high reflectivity were also observed by two S-band radars (Figure 4g,h), while the corresponding reflectivity observed by XPRAD (Figure 4e) is relatively lower. The overall differential reflectivity observed by XPRAD is impacted by attenuation and systematic bias that causes underestimation in region A. Figure 4d and f show corrected Z_h and Z_{dr} images obtained from the correction algorithm for rain attenuation. Compared to the Figure 4e, the weak reflectivity in region A shown in Figure 4f has now been increased up to 35 dBZ above, owing to the attenuation correction. These corrected Z_h values are now similar to those observed by the S-band radar and are in good consistency with the K_{dp}. The measured large Z_{dr} values in Figure 4c have also been corrected, authentic light rainfall has approximated zero dB of Z_{dr}. Thus, the Z_h and Z_{dr} after correction are consistent with the K_{dp} pattern (Figure 4b), which is not affected by attenuation.

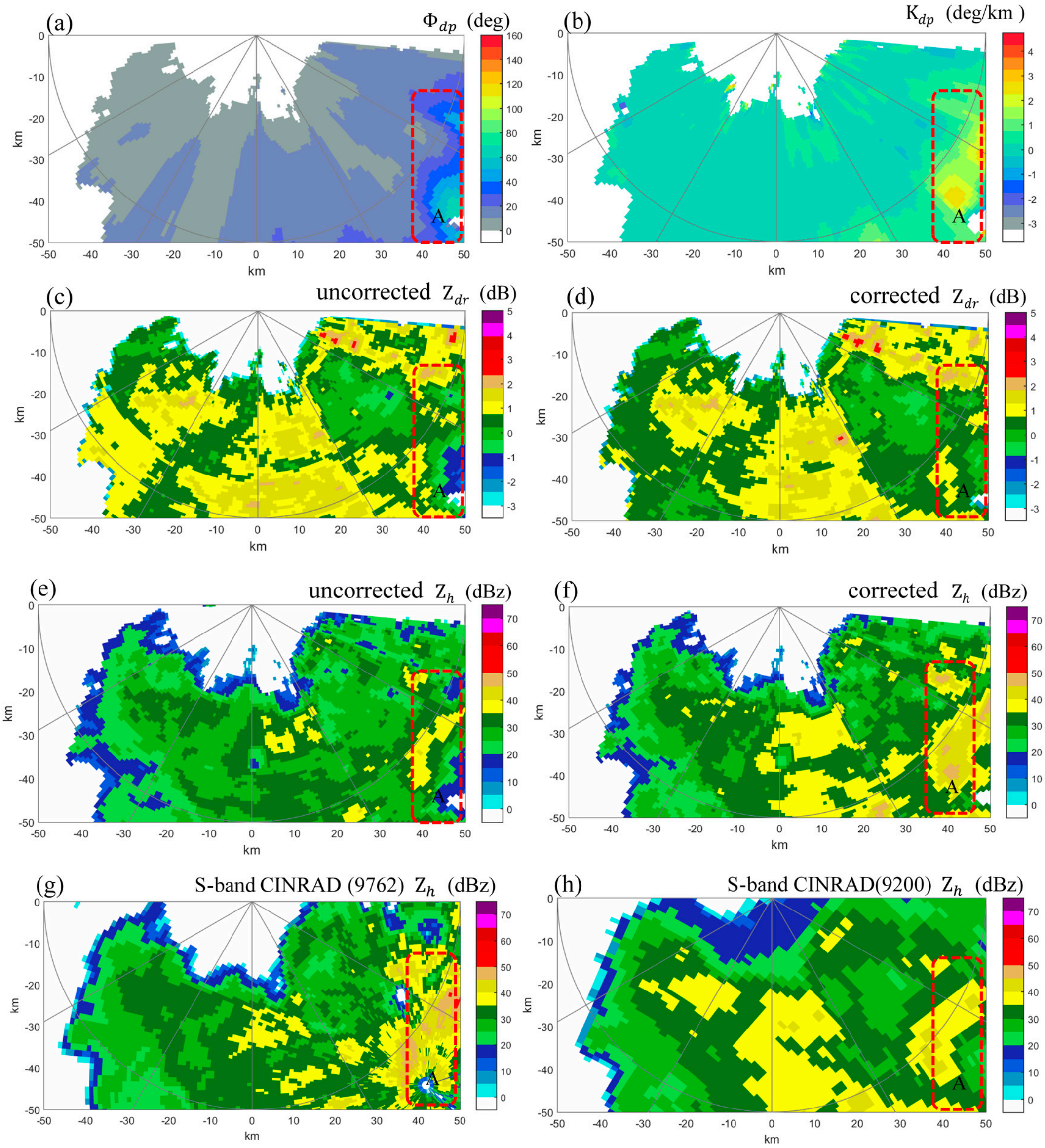

Figure 4. PPI images of polarimetric variables observed at an elevation angle of 2.5°, at 11:57 (BJT) on 5 June 2016: (**a**) Φ_{dp}; (**b**) K_{dp}; (**c**) uncorrected Z_{dr}; (**d**) corrected Z_{dr}; (**e**) uncorrected Z_h; (**f**) corrected Z_h; (**g**) S-band CINRAD (9762) Z_h; (**h**) S-band CINRAD (9200) Z_h. The red dashed rectangle A indicates the region with strong rainfall where the attenuation for the X-band happened heavily.

Furthermore, to validate the overall performance of attenuation correction, the scattergram comparisons of K_{dp} versus Z_h, Z_{dr} versus Z_h, and K_{dp}/Z_{hl} (Z_{hl} is in the linear unit of mm^6m^{-3}) versus Z_{dr} for all fifteen rainfall events at LongMen station are performed to investigate the efficiency of attenuation correction (see Figure 5). The comparisons with the attenuation uncorrected Z_h and Z_{dr}

values are presented in the left panels, while the right panels are for the attenuation corrected values. The radar data points in the figures are from the PPI at the elevation angle of 0.5° of rainfall events. The black asterisks along with the colored density scatters are the simulated radar moments using raindrop spectra data. It is shown in Figure 5a that, for a given K_{dp}, the uncorrected Z_h values are much smaller than those expected from the corrected K_{dp}–Z_h relations (Figure 5b). Similar patterns are also observed in the comparisons of Z_{dr} versus Z_h (Figure 5c,d) and K_{dp}/Z_{hl} versus Z_{dr} (Figure 5e,f). Figure 5d also shows that the bias of Z_{dr} exists as light Z_h ranging from 5 to 15 dBZ corresponding to a non–zero mean value of Z_{dr}, which did not qualify well the principle of 'light rain at low angle'. The existence of a tiny bias is normal, since the balance of two channels may vary along time. Compared with the DSD-simulated radar moments, the XPRAD radar observations visually keep the consistency with the theoretical simulation.

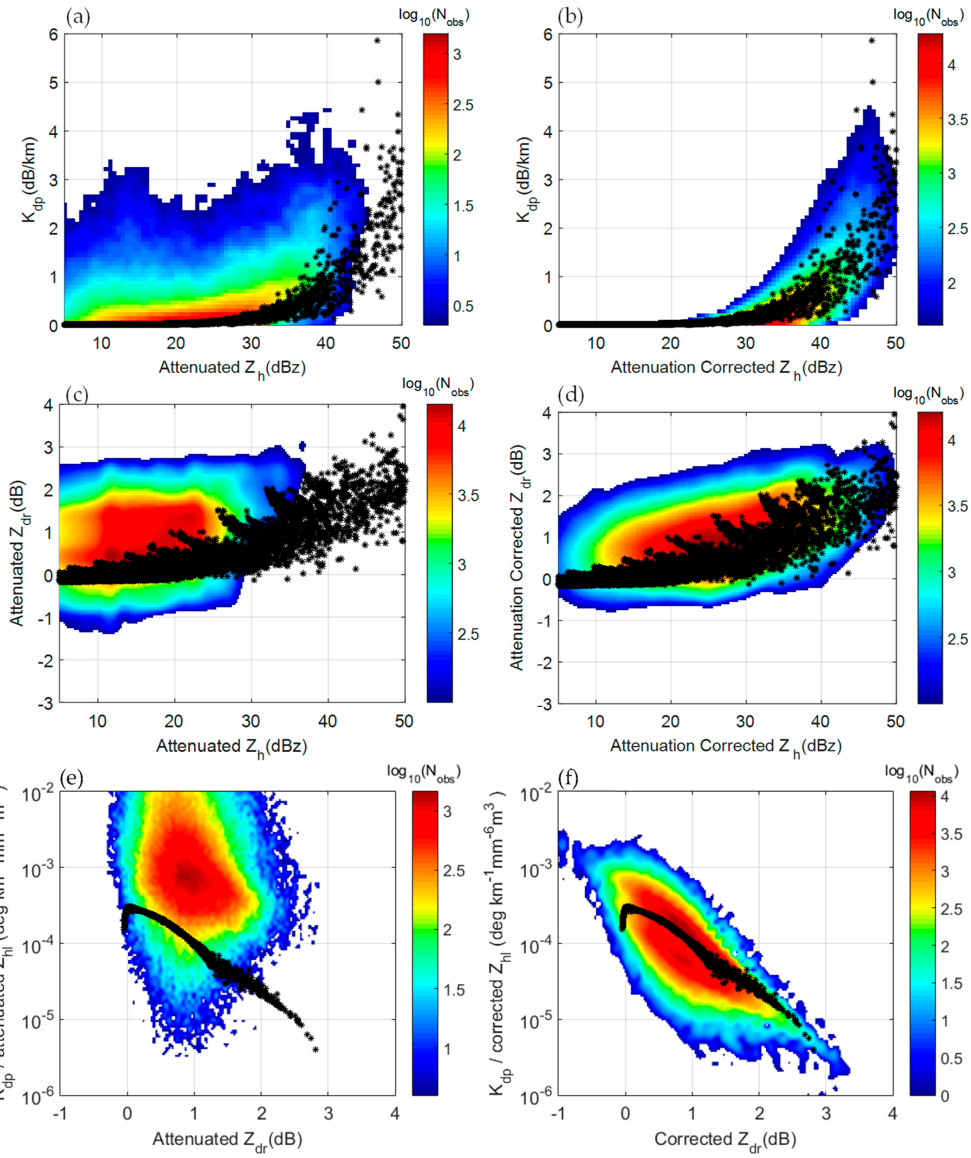

Figure 5. Scatterplots of K_{dp} vs. Z_h, Z_{dr} vs. Z_h and K_{dp}/Z_{hl} vs. Z_{dr} for fifteen rainfall events, Z_{hl} is the linear form of Z_h, the black asterisks along with the color coded density scatters are radar moments computed based on DSD data: (**a**) comparisons between K_{dp} and attenuated Z_h; (**b**) K_{dp} and attenuation corrected Z_h; (**c**) attenuated Z_{dr} and Z_h; (**d**) attenuation corrected Z_{dr} and Z_h; (**e**) K_{dp}/Z_{hl} versus Z_{dr} before attenuation correction; (**f**) K_{dp}/Z_{hl} versus Z_{dr} after attenuation correction.

3.3. Assessment of Z_{dr} and Z_h Measurement Biases

3.3.1. Z_{dr} Bias Assessment

The gain and loss differences between the horizontal and vertical channel induce systematic bias in the Z_{dr} estimate. The accuracy of Z_{dr} with 0.2 dB is required for the application of QPE or hydrometeor classification [17] and self-consistency process, therefore, careful absolute calibration is necessary. The two methods for Z_{dr} bias correction are employed here considering the respective strengths and limitations.

Light rain at low angle **(LRLA)**. The shape of large-sized free-falling rain drops are modeled as non-spherical oblate spheroids [22]. This is the result of forces and surface tension acting around the drops. Moreover, rain drops with a diameter size less than 0.5 mm can be modeled using a nearly spherical shape. This inherent microphysical property of small drops can be used to estimate the Z_{dr} bias. Due to the spherical shape of small drops (raindrop axis ratio ≈ 1), the power return from both polarizations (horizontal and vertical) is expected to be identical. This will lead to an expected measured mean Z_{dr} of approximately 0 dB plus/minus the estimated radar measurement bias. The mean Z_{dr} was estimated only using the pixels with ρ_{hv} greater than 0.95, SNR greater than 10 dB Z_h ranging from 10 to 15 dBZ. Besides, rainfall over the radome can induce signal attenuation and lead to the uncertainty of bias estimation. The data at times without rain over the radar radome were selected for assessing the systematic bias. Figure 6 shows an example scatter of Z_h versus Z_{dr} captured at 1.5° elevation angle of one rainfall event at 16:25 (BJT) on 4 June 2016. It can be seen from the plot that the mean Z_{dr} increases exponentially with Z_h. For this case, the average bias is 0.481 dB.

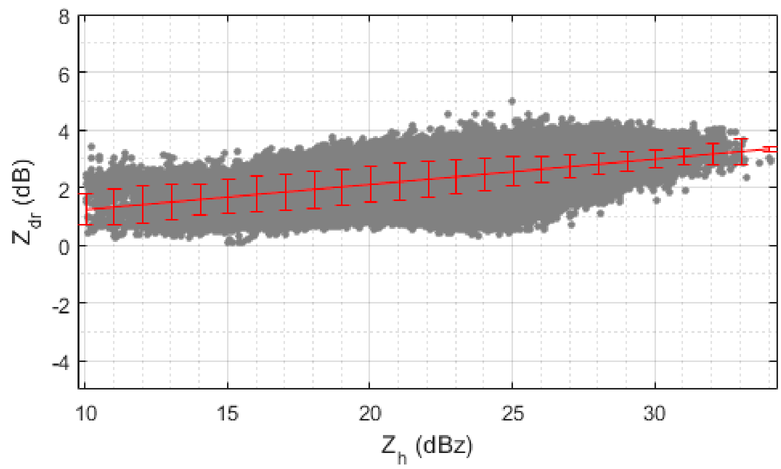

Figure 6. An example case of Z_h and Z_{dr} scatter plot and best polynomial fit for the XPRAD radar data for a rainfall event at 16:25 (BJT) on 4 June 2016. A bias of 0.481 dB was deducted from the Z_{dr} data to perform the calibration.

Dry aggregated snow **(DAS)**. The average Z_{dr} values of aggregated snow normally do not exceed 0.25 dB and tend to slowly decrease with increasing Z_h [17]. Considering the low variability of the expected power returns from dry aggregated snowflakes between the S- and X-band, the estimated value of 0.2 dB accounts for the absolute calibration of Z_{dr} at X-band [18]. Dry aggregated snowflakes are universally present above the melting layer in stratiform clouds. The existence and identification of bright bands becomes the prerequisite for calibration using 'dry aggregated snow' method. A number of polarimetric observations show that the aggregated snow likely occurs around 1–2 km above the bright band [27]. Figure 7 represents a vertical profile example case of Z_h, Z_{dr}, and ρ_{hv} from the stratiform precipitaon at 16:25 (BJT) on 4 June 2016. ρ_{hv} is the main polarized variable which can be used to identify the melting layer and freezing-level heights, and discriminating among rain, snow, and melting-level regions. The magnitude of ρ_{hv} is generally in the range of 0.7 to 0.95 in the melting layer. For this case, a ρ_{hv} lower than 0.8 was observed at the melting layer where the height is 3.3 km. Upon this, the average value Z_{dr} at the height between 4.3 and 5.3 km was approximate to the systematic bias, which is about 0.52 dB and nearly equal to that estimated by the 'light rain at low angle' approach for the same case.

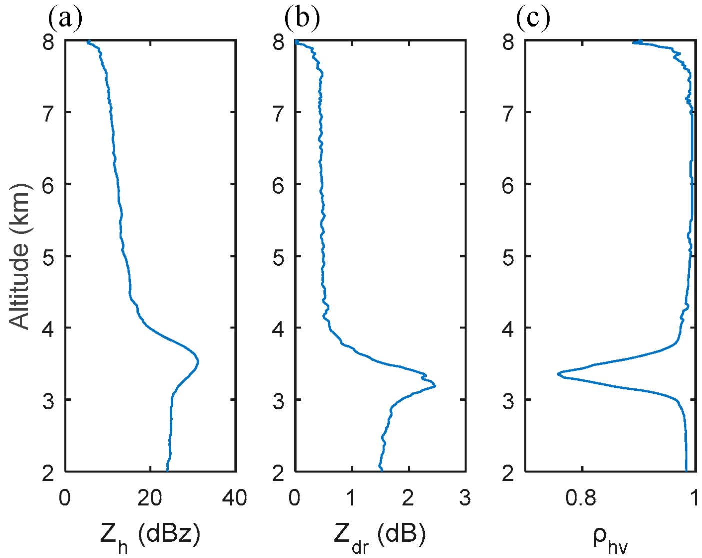

Figure 7. Vertical profile of polarized variables for one stratiform precipitation at 16:25 (BJT) on 4 June 2016. (**a**) Z_h; (**b**) Z_{dr}; (**c**) ρ_{hv}. Three polarized variables are combined to identify the melting layer and dry snow. The mean Z_{dr} of dry snow for this case is 0.52 dB.

Two approaches were applied for the whole rainfall event to estimate daily Z_{dr} bias. The 'light rain at low angle' approach was eligible for all of the rainfall events. The 'dry aggregated snow' approach was performed only for the stratiform rainfall event, considering that dry snow is hardly identified for convective rainfall. There were six stratiform rainfall processes for fifteen rainfall events. Table 4 shows the mean and standard deviation of the Z_{dr} bias estimated by the DAS and LRLA approaches for all rainfall events.

Several characteristic of Z_{dr} bias over IOP can be found from Table 4, such as: (1) The mean of the Z_{dr} bias estimated by the 'dry aggregated snow' approach and the 'light rain at low angle' approach varied from 0.52 dB to 0.79 dB, and from 0.43 dB to 0.81dB, respectively, The standard deviation of Z_{dr} bias estimated by the 'dry aggregated snow' approach and the 'light rain at low angle' approach varied from 0.13 dB to 0.22 dB, and from 0.17 to 0.32 dB, respectively; (2) The changing trend of Z_{dr} bias can be seen as slightly increasing from both approaches.; (3) The 'dry aggregated snow' approach has a lower estimate standard deviation than the 'light rain at low angle' approach; (4) The overall average of Z_{dr} bias is 0.68 dB and 0.65 dB, respectively, for the DAS and LRLA approach.

Based on the quantitative bias assessment, the biased Z_{dr} can be corrected as:

$$Z_{dr} = Z_{drm} - Z_{dr(bias)} \tag{15}$$

where Z_{drm} is measured differential reflectivity, $Z_{dr(bias)}$ is averaged bias for each event, and bias correction was performed with separate $Z_{dr(bias)}$ for each rainfall event.

Table 4. Mean and standard deviation of Z_{dr} bias estimated by the DAS [1] and LRLA [2] approaches for all rainfall events.

Rainfall Event No.	Mean of Z_{dr} Bias (dB)		Standard Deviation of Z_{dr} Bias (dB)	
	DAS Approach	LRLA Approch	DAS Approach	LRLA Approch
1	0.52	0.43	0.13	0.18
2	—	0.48	—	0.17
3	0.75	0.52	0.15	0.19
4	—	0.53	—	0.21
5	0.65	0.65	0.16	0.21
6	0.63	0.65	0.15	0.30
7	—	0.61	—	0.20
8	—	0.60	—	0.25
9	—	0.68	—	0.17
10	—	0.69	—	0.18
11	—	0.76	—	0.24
12	—	0.75	—	0.22
13	0.79	0.78	0.22	0.21
14	—	0.79	—	0.22
15	0.77	0.81	0.21	0.32

[1] DAS is the acronym of 'dry aggregated snow'. [2] LRLA is the acronym of 'light rain at low angle'.

3.3.2. Z_h Bias Assessment

The self-consistency principle claim that the polarimetric variables of Z_h, Z_{dr} and K_{dp} lie in a limited 3-D space for rain medium [20]. As such, K_{dpc} measurements can be reconstructed from Z_h and Z_{dr} measurements, as defined below.

$$K_{dpc} = aZ_{hl}^{b}Z_{drl}^{c} \tag{16}$$

where K_{dpc} represents the specific differential phase reconstructed from Z_h and Z_{dr}, Z_{hl} and Z_{drl} are in linear units. Before reconstruction, Z_{dr} is corrected for attenuation and bias, and Z_{dr} is corrected for attenuation. Two methods were evaluated for Z_{dr} bias correction: the intrinsic properties of dry aggregated snow present above the melting layer, and light rain measurements close to the ground. The parameters a, b, and c depend on the size, shape, and distribution of raindrops and can be calculated using rain simulations with a gamma DSD and a fixed drop axis ratio relationship. The bias $Z_{h(bais)}$ in Z_h can be obtained using the following relationship:

$$Z_{h(bias)} = \frac{10}{b}\log_{10}\left(\frac{K_{dpm}}{K_{dpc}}\right) \tag{17}$$

where K_{dpm} is the computed specific differential phase obtained from the measured radar differential phase.

The self-consistency principle was applied for the fifteen rainfall events. Based on the radar variables simulated from the in-site raindrop spectra data, the parameters a, b, and c were regressed as 2.22×10^{-4}, 1, and -4.58, respectively, shown in It is worthwhile noting that the exponent β and ρ are close to unity, and the linearity has a good approximation at frequencies from 2.8 to 9.3 GHz [25,26]. Due to the variation of raindrop shape, the coefficient α varies from 0.139 to 0.335 dB/deg and the coefficient γ also varies from 0.114 to 0.174 dB/deg. The variation differences of β or ρ influenced by temperature is much smaller than that of coefficient α or γ. The uncertainty of α and γ accounts for 28% or 17% relative errors to the mean value respectively [12]. The simulations for $A_h - K_{dp}$ and $A_{dp} - A_h$ were performed as shown in the scatterplot of Figure 3. Through nonlinear regression processing, α and γ here are 0.323 and 0.131, β and ρ are 1.05 and 1.2, as shown in Table 3. The correlation coefficient between A_h and K_{dp}, A_{dp} and A_h is 0.99 and 0.96, respectively, and indicates that the empirical relations are eligible for attenuation correction at the X band, based on the self-consistent method.

With the attenuation and bias corrected Z_{dr} and retrieved K_{dp}, the Z_h bias assessment using the self-consistency principle was performed for rainfall events. In order to validate the efficiency of self-consistency-based bias assessment, it was performed to compare XPRAD and the two closest S-band CINRAD radars (9200 and 9762) that were supposed to be well-calibrated. To perform the X-band and S-band data comparison, scatter plots of Z_S (Z_h from S-band) versus Z_X (Z_h from X-band) were generated for the same radial direction at the elevation of 0.5°, shown as Figure 8a,b. Terrain height changing between the X- and S-band radar is also considered with the usage of the DEM (digital elevation model) data, shown as green color padding in Figure 8a,b. There is some slight terrain blockage for CINRAD (9200) at the azimuth of 35°. The beam blockage ratio (BBR) was calculated with the method described in [28]. The BBR along this radial varies from 0.03 to 0.24, and the reflectivity was compensated with the BBR calculation.

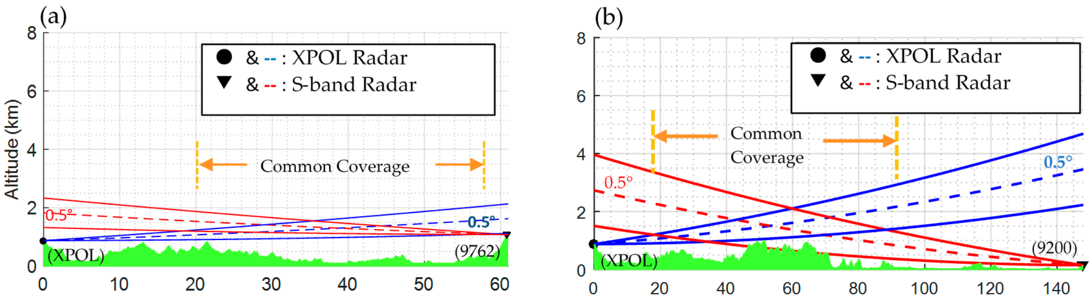

Figure 8. Reflectivity comparisons in common radial coverage between XPRAD and S-band CINRADs at the elevation of 0.5°. (**a**) spatial illustration of common radial coverage between XPRAD and CINRAD (9762), azimuth at 137° for XPRAD, azimuth at 317° for CINRAD (9762); (**b**) Same illustration like (**a**) between XPRAD and CINRAD (9200), azimuth at 215° for XPRAD, azimuth at 35° for CINRAD (9200).

For radar data selection, only 0.5° PPI scans with a data collection time difference of less than 1 min were selected. Pixels where both the S- and X-band data coexist within a Z_h value in the range of 15 dBZ to 45 dBZ were selected to limit the errors due to uncertainty in low Z_h returns and the deviation from Rayleigh scattering of big drops from high Z_h returns in the X-band data. Figure 8a,b shows the common radial coverage area at the elevation of 0.5° between the S-band radar and the X-band radar along the same radial direction. The S-band range bin length was 250 m, the X-band range bin length was 75 m. The common range bin step was 750 m. Within the common radial range, the reflectivity at every 750 m interval for the common coverage of both radar was selected. After the data pixel selection was performed, the mean Z_S and mean Z_X values were computed for each radar separately for all the available reflectivity values from the PPI scan at the elevation of 0.5°.

To estimate the reflectivity bias between the CINRAD and XPRAD, the following statistical approach was used:

$$\Delta Z = \frac{1}{n}\sum(Z_S - Z_X) \tag{18}$$

where n represents the number of Z_h meeting the selection condition for each radar throughout each rainfall event, Z_X is the reflectivity from XPRAD and just corrected for attenuation prior to bias correction with self-consistency processing, Z_s is the reflectivity from CINRAD.

The Z_h bias estimated by the self-consistency approach and the two closest CINRAD are shown in Table 5. There are no comparison outcomes between CINRAD and XPRAD for rainfall event number 4, 10, 11 and 14, since the corresponding rainfall event did not occur at the common radial coverage. The Z_h bias estimated by the self-consistency approach, CINRAD (9200) and CINRAD (9762) varies from 0.10 dBZ to 1.38 dBZ, from 0.11 dBZ to 1.23 dBZ, and from 0.15 dBZ to 1.41 dBZ, respectively. The overall average Z_h bias estimated by the self-consistency approach, CINRAD (9200) and CINRAD (9762) is 0.60 dBZ, 0.65 dBZ, and 0.75 dBZ, respectively. The maximum Z_h bias estimated is 1.41 dBZ, less than 1.5 dBZ. The maximum standard deviation of Z_h bias estimated is 0.48 dBZ, less than 0.5 dBZ.

Such small differences demonstrate the feasibility of the application of the self-consistency criterion in a dual polarization radar measurement quality check.

Table 5. Mean and standard deviation of Z_h bias by the self-consistency approach and the two closest CINRAD.

Rainfall Event No.	Mean of Z_h Bias (dB)			Standard Deviation of Z_h Bias (dB)		
	Self-Consistency	CINRAD (9200)	CINRAD (9762)	Self-Consistency	CINRAD (9200)	CINRAD (9762)
1	0.10	0.31	1.1	0.08	0.18	0.19
2	0.19	0.33	0.15	0.12	0.24	0.15
3	0.25	0.28	0.83	0.12	0.25	0.24
4	0.14	0.95	—	0.16	0.19	—
5	0.19	0.56	0.50	0.18	0.18	0.24
6	0.93	1.23	1.41	0.33	0.48	0.18
7	0.97	0.78	0.69	0.38	0.32	0.23
8	0.96	0.98	0.48	0.38	0.37	0.19
9	0.96	0.11	0.74	0.37	0.24	0.20
10	1.38	—	—	0.39	—	—
11	1.05	—	—	0.37	—	—
12	0.61	0.72	0.96	0.12	0.27	0.38
13	0.39	0.30	0.28	0.21	0.36	0.20
14	0.40	—	0.76	0.20	—	0.12
15	0.35	1.25	1.1	0.19	0.26	0.13

Based on the quantitative assessment, the biased Z_h can be corrected with a self-consistency estimation, as:

$$Z_h = Z_{hm} + Z_{h(bais)} \tag{19}$$

where Z_{hm} is the measured reflectivity, $Z_{dr(bias)}$ is the averaged bias for each event, and bias correction was performed with a separate $Z_{dr(bias)}$ for each rainfall event.

4. Rainfall Performance during SCMREX

4.1. Rainfall Algorithms

Based on the physical principle of precipitation, the rainfall rate can be represented by DSD density, defined as:

$$R = 0.6\pi \times 10^{-3} \int v(D) D^3 N(D) dD \tag{20}$$

where $v(D)$ is the raindrop terminal velocity in the unit of ms^{-1}, D is the raindrop diameter in mm, $N(D)$ is the DSD density in the unit of $\text{m}^{-3}\text{mm}^{-1}$.

For a given DSD dataset, a variety of empirical rainfall relationships between the polarimetric variables and rainfall rate can be derived via nonlinear regression. In this study, $R(Z_h, Z_{dr})$ and $R\left(K_{dp}\right)$ were estimated to validate the self-consistency and QPE performance for XPRAD. Herein, $R(Z_h, Z_{dr})$ is fundamentally a power-based relation, whereas $R\left(K_{dp}\right)$ is a phase-based method. Meanwhile, a CINRAD-based QPE was also performed. The relation of $R(Z_h)$ was widely adopted for CINRAD, since many CINRADs are a single horizontal polarization radar.

The rainfall rate (R) versus the K_{dp}, Z_h and Z_{dr} for the X-band are simulated from in-site raindrop spectra data based on the T-matrix approach under the simulation conditions described in Section 3.1. The scatter density plot of R versus K_{dp} is drawn in Figure 9a. The best fit power law relation for R-K_{dp} is regressed as shown in Figure 9a by a red line. The scatterplot of R versus Z_h and Z_{dr} is shown in Figure 9b by a gray square, and the best fit power law relation for R versus Z_h, Z_{dr} was also regressed and is shown by the colored three-dimensional mesh. The specific parameters of the rainfall algorithms were obtained as:

$$R\left(K_{dp}\right) = 15.1K_{dp}^{0.92};\ (\text{X-band}) \tag{21}$$

$$R(Z_h, Z_{dr}) = 0.009 \times 10^{(0.1 \times Z_h - 0.458 \times Z_{dr})};\ (\text{X-band}) \tag{22}$$

where, Z_h is in the unit of dBZ, and Z_{dr} is in the unit of dB. The rainfall rate (R) versus the Z_h for the S-band is also simulated from raindrop spectra data with the T-matrix method, and the best-fit power low relation to determine the coefficients for $R(Z_h)$ is regressed as shown in Figure 10. The specific parameters of the rainfall algorithms are obtained as

$$R(Z_h) = 0.0216 \times 10^{(0.069 \times Z_h)};\ (\text{S-band}) \tag{23}$$

It should be noted that the relations in Equations (21)–(23) are particularly suited for the region in Guangdong province.

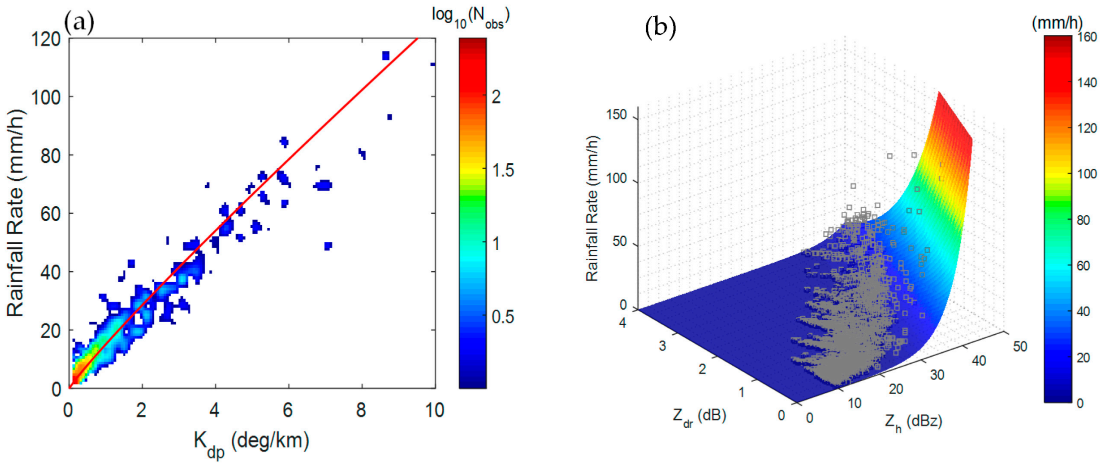

Figure 9. Scattergram of the DSD-estimated rainfall rate (R), Z_h, Z_{dr} and K_{dp} for fifteen rainfall events. (**a**) K_{dp} versus R, the red solid line is the best-fitted power-law of $R(K_{dp})$; (**b**) Z_h, Z_{dr} versus R, the grey square represents the triplet of DSD-estimated R, Z_h and Z_{dr}, the three-dimensional colored surface is the best fitted power-law relation of $R(Z_h, Z_{dr})$.

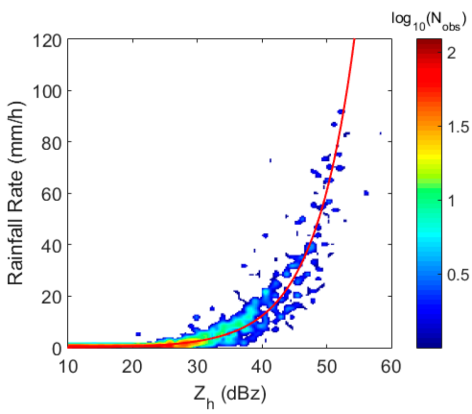

Figure 10. Scattergram of DSD-estimated rainfall rate (R) and Z_h for CINRAD. The red solid line is the best-fitted power-law of $R(Z_h)$.

4.2. Performance Evaluation

In order to demonstrate the XPRAD performance for QPE, the rainfall records from a rain gauge network, which consists of six gauges, were used for evaluation purposes. The gauge network is deployed and managed by the Guangdong Meteorological Bureau. For the sake of cross comparisons, we aggregated the rainfall data to rainfall accumulations in 1.0-, 2.0- and 3.0-h intervals. The radar measurements were spatially chosen at the location of the rain gauges for validation. For the sake of quantifying the accuracy of XPRAD rainfall products, the fractional standard error (*FSE*), normalized mean bias (*NMB*) and correlation coefficient (*CORR*) of the rainfall amount at different time scales were computed for $R(Z_h, Z_{dr})$, $R(K_{dp})$ and $R(Z_h)$ defined as:

$$FSE = \frac{\sqrt{\frac{1}{N}\sum_i^N (\mathrm{r}_i - \mathrm{g}_i)^2}}{\frac{1}{N}\sum_i^N \mathrm{g}_i} \times 100\% \tag{24}$$

$$NMB = \frac{\frac{1}{N}\sum_i^N (\mathrm{r}_i - \mathrm{g}_i)}{\frac{1}{N}\sum_i^N \mathrm{g}_i} \times 100\% \tag{25}$$

$$CORR = \frac{\sum_i^N (\mathrm{g}_i - \overline{\mathrm{g}})(\mathrm{r}_i - \overline{\mathrm{r}})}{\sqrt{\sum_i^N (\mathrm{g}_i - \overline{\mathrm{g}})^2}\sqrt{\sum_i^N (\mathrm{r}_i - \overline{\mathrm{r}})^2}} \tag{26}$$

where *FSE* and *NMB* are in percent, *CORR* is dimensionless, r_i and g_i represent the rainfall accumulation from radar and gauge, N is the total sampling number.

The *NMB* and *FSE* results, as well as the mean values of the gauge rainfall measurement at different time scales (i.e., 1-, 2- and 3-h) for each of the events, are shown in Table 6. In addition, the overall *NMB* and *FSE* were calculated, at each time scale, based on the entire observation combining all the fifteen events. The main findings from the evaluation results of different rainfall products are summarized as follows:

(1) The *FSEs* of the $R(Z_h, Z_{dr})$ are 71.37%, 68.98%, and 62.22% for 1-, 2- and 3-h rainfall accumulations, respectively, and the *NMBs* are −13.62%, −3.1%, and 0.04%, respectively. The *FSEs* of the $R(K_{dp})$ are 79.77%, 57.95%, 50.75%, for 1-, 2- and 3-h rainfall accumulations, respectively, and the *NMBs* are −10.65%, −4,84%, and −2.64%, respectively. The *NMBs* and *FSEs* of $R(K_{dp})$ estimated for XPRAD are approximate to those estimated for CINRAD. The performance is further demonstrated by the combined scatter plots shown in Figure 11.

(2) Although the $R(K_{dp})$ shows slightly better performance than $R(Z_h, Z_{dr})$, the difference is not remarkable. This also implies that attenuation and bias correction are critical for X-band QPE applications.

(3) It can also be seen that the *FSEs* of the rainfall estimate relations show a decreasing trend as the rainfall accumulation time increases from 1 h to 3 h, inversely the *CORR* of the rainfall estimate relations had an increasing trend. This is because the random radar measurement errors are being reduced by temporal averaging.

Table 6. Assessment of $R(K_{dp})$, $R(Z_h, Z_{dr})$ and $R(Z_h)$ for fifteen rainfall events under four scales of accumulated time interval.

Time Scale (Hour)	**FSE (%)**				**NMB (%)**				***CORR***			
	XPRAD $\boldsymbol{R(Z_h, Z_{dr})}$	***XPRAD*** $\boldsymbol{R(K_{dp})}$	***9200*** $\boldsymbol{R(Z_h)}$	***9762*** $\boldsymbol{R(Z_h)}$	***XPRAD*** $\boldsymbol{R(Z_h, Z_{dr})}$	***XPRAD*** $\boldsymbol{R(K_{dp})}$	***9200*** $\boldsymbol{R(Z_h)}$	***9762*** $\boldsymbol{R(Z_h)}$	***XPRAD*** $\boldsymbol{R(Z_h, Z_{dr})}$	***XPRAD*** $\boldsymbol{R(K_{dp})}$	***9200*** $\boldsymbol{R(Z_h)}$	***9762*** $\boldsymbol{R(Z_h)}$
1.0	71.37	79.77	69.75	72.58	−13.62	−10.65	−13.84	−11.78	0.87	0.86	0.92	0.91
2.0	68.98	57.95	60.45	51.08	−3.10	−4.84	−11.12	−4.91	0.89	0.91	0.91	0.93
3.0	62.22	50.75	52.11	41.30	0.04	−2.64	−12.55	−2.33	0.90	0.92	0.91	0.94

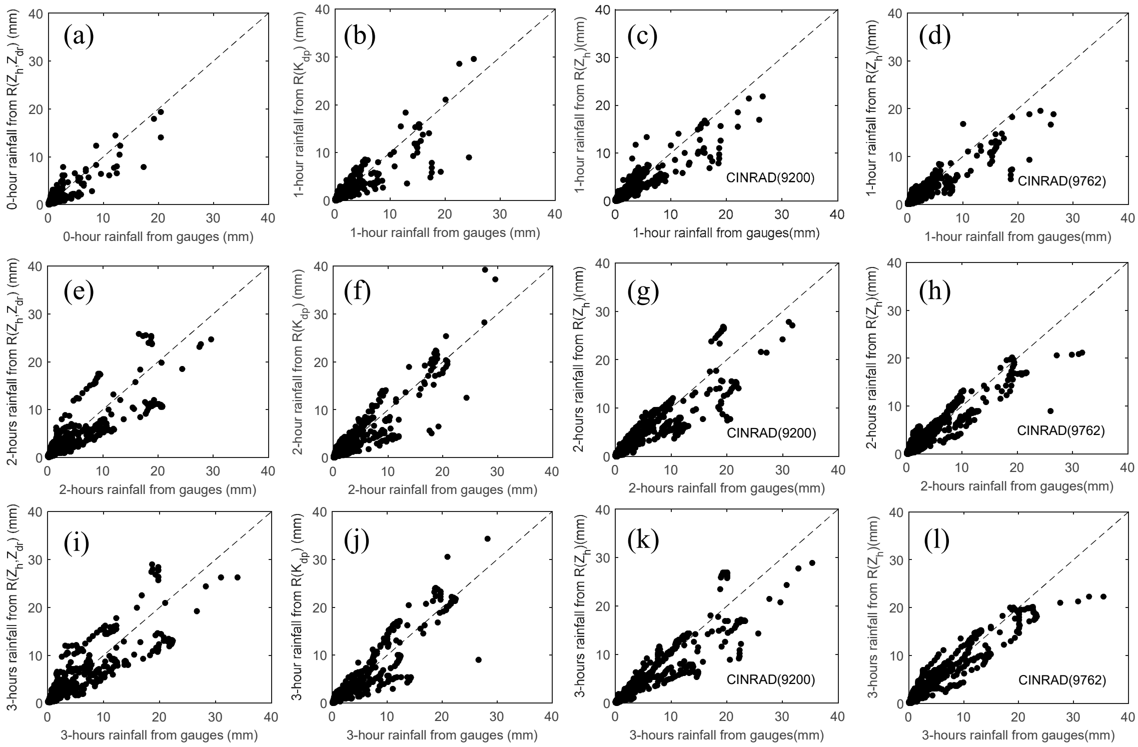

Figure 11. Scatterplots of radar rainfall estimate versus rain gauge for all events. (**a**) 1-h (**e**) 2-h (**i**) 3-h of $R(Z_h, Z_{dr})$-based rainfall accumulations for XPRAD; (**b**) 1-h (**f**) 2-h (**j**) 3-h of $R(K_{dp})$-based rainfall accumulations for XPRAD; (**c**) 1-h (**g**) 2-h (**k**) 3-h of $R(Z_h)$-based rainfall accumulations for CINRAD(9200); (**d**) 1-h (**h**) 2-h (**l**) 3-h of $R(Z_h)$-based rainfall accumulations for CINRAD(9200).

5. Summary and Conclusions

Endorsed by the World Meteorological Organization (WMO) World Weather Research Program (WWRP), the China Meteorological Administration (CMA) has initiated the SCMREX field experiment to facilitate the efforts in improving QPE/QPF during the pre-summer rainy season in southern China. The X-band XPRAD radar is deployed as part of the integrated observing network of SCMREX during the intensive observation periods, aiming to fill the gaps of the operational S-band weather radar coverage and provide high resolution observations through its flexible scan strategy.

However, the X-band deployment did not come easily, as technical solutions need to be found for several issues including attenuation correction. This paper takes advantage of the dual-polarization technique, particularly the differential phase measurements that are not affected by radar calibration and attenuation, to quantitatively correct attenuation and systematic biases on Z_h and Z_{dr}. The XPRAD radar data collected for fifteen rainfall events during the intensive observation period in 2016 were investigated to demonstrate the data quality and rainfall performance.

It is concluded that the Z_{dr} bias varies within a mean value of 0.68 dB. The calibration accuracy of Z_{dr} is less than 0.2 dB. Both the self-consistency-based calculation and the cross-validation between the S-band radar observations show that the Z_h observed by XPRAD has a mean bias value less than 1.6 dBZ and a standard deviation less than 0.5 dBZ. The 1-, 2- and 3-h rainfall accumulations derived using $R(K_{dp})$ and $R(Z_h, Z_{dr})$ agree well with the rain gauge measurements and the CINRAD-based rainfall estimation, which demonstrates the good performance of the XPRAD radar for QPE. The XPRAD product evaluation showed that the $R(K_{dp})$-based algorithm had lower overall biases of −10.65%, −4,84% and −2.64%, and a higher correlation coefficient of 0.86, 0.91 and 0.92, for 1-, 2- and 3-h rainfall accumulations, respectively. It is worth noting that $R(Z_h, Z_{dr})$ showed similar performance to $R(K_{dp})$, if Z_h and Z_{dr} were well-corrected. The SCMREX field campaign was extended to 2018 by the WMO and future studies with XPRAD will focus on DSD retrieval and the classification of different hydrometeor types for pre-summer precipitation over southern China.

Acknowledgments: This research was financially supported by the National Natural Science Foundation of China (No. 41505031), China Scholarship Council (No. 201508515021), Scientific Research Funding of CUIT (No. J201603), and Funding from China Meteorological Administration Sounding Engineering Technology Research Centre. The participation of H.C. and V.C. was supported by the National Science Foundation Hazards SEES program. The authors would like to thank Fangqiang Wei for giving us many constructive suggestions. We want to acknowledge Guangdong Meteorological Bureau and Chinese Academy of Meteorological Sciences for providing respectively rain gauge data and raindrop spectra data used in this study.

Author Contributions: Z.S. performed the experiments and data analysis. Z.S. and H.C. analyzed the results and prepared the manuscript. V.C. supervised the work and provided critical comments. J.H. provided comments on the results and reviewed the manuscript.

Conflicts of Interest: The authors declare no conflict of interest.

References

1. Luo, Y.; Zhang, R.; Wan, Q.; Wang, B.; Wong, W.K.; Hu, Z.; Xiao, Y. The Southern China Monsoon Rainfall Experiment (SCMREX). *Bull. Am. Meteorol. Soc.* **2017**, *98*, 999–1013. [CrossRef]
2. McLaughlin, D.; Pepyne, D.; Philips, B.; Kurose, J.; Zink, M.; Westbrook, D.; Kollias, P. Short-Wavelength Technology and the Potential For Distributed Networks of Small Radar Systems. *Bull. Am. Meteorol. Soc.* **2009**, *90*, 1797–1817. [CrossRef]
3. Chandrasekar, V.; Chen, H.; Philips, B. Principles of High-Resolution Radar Network for Hazard Mitigation and Disaster Management in an Urban Environment. *J. Meteorol. Soc. Jpn.* **2018**, *96A*, in press. [CrossRef]
4. Chandrasekar, V.; Wang, Y.; Chen, H. The CASA quantitative precipitation estimation system: A five year validation study. *Nat. Hazards Earth Syst. Sci.* **2012**, *12*, 2811–2820. [CrossRef]
5. Matrosov, S.Y.; Kingsmill, D.E.; Martner, B.E.; Ralph, F.M. The utility of X-band polarimetric radar for quantitative estimates of rainfall parameters. *J. Hydrometeorol.* **2005**, *6*, 248–262. [CrossRef]
6. Anagnostou, M.N.; Anagnostou, E.N.; Vivekanandan, J.; Ogden, F.L. Comparison of raindrop size distribution estimates from X-band and S-band polarimetric observations. *IEEE Geosci. Remote Sens. Lett.* **2007**, *4*, 601–605. [CrossRef]
7. Kim, D.-S.; Maki, M. Validation of composite polarimetric parameters and rainfall rates from an X-band dual-polarization radar network in the Tokyo metropolitan area. *Hydrol. Res. Lett.* **2012**, *6*, 76–81. [CrossRef]
8. Chen, H.; Lim, S.; Chandrasekar, V.; Jang, B.-J. Urban Hydrological Applications of Dual-Polarization X-Band Radar: Case Study in Korea. *J. Hydrol. Eng.* **2017**, *22*, E5016001. [CrossRef]
9. Testud, J.; Bouar, E.L.; Obligis, E.; Ali-Mehenni, M. The Rain Profiling Algorithm Applied to Polarimetric Weather Radar. *J. Atmos. Ocean. Technol.* **2000**, *17*, 332–356. [CrossRef]
10. Matrosov, S.Y.; Clark, K.A.; Martner, B.E.; Tokay, A. X-band polarimetric radar measurements of rainfall. *J. Appl. Meteorol.* **2002**, *41*, 941–952. [CrossRef]
11. Zrnic, D.S.; Ryzhkov, A.V. Polarimetry for weather surveillance radars. *Bull. Am. Meteorol. Soc.* **1999**, *80*, 389–406. [CrossRef]
12. Park, S.; Bringi, V.; Chandrasekar, V.; Maki, M.; Iwanami, K. Correction of radar reflectivity and differential reflectivity for rain attenuation at X band. Part I: Theoretical and empirical basis. *J. Atmos. Ocean. Technol.* **2005**, *22*, 1621–1632. [CrossRef]
13. Park, S.; Maki, M.; Iwanami, K.; Bringi, V.; Chandrasekar, V. Correction of radar reflectivity and differential reflectivity for rain attenuation at X band. Part II: Evaluation and application. *J. Atmos. Ocean. Technol.* **2005**, *22*, 1633–1655. [CrossRef]
14. Gorgucci, E.; Chandrasekar, V.; Baldini, L. Correction of X-band radar observation for propagation effects based on the self-consistency principle. *J. Atmos. Ocean. Technol.* **2006**, *23*, 1668–1681. [CrossRef]
15. Kalogiros, J.; Anagnostou, M.N.; Anagnostou, E.N.; Montopoli, M.; Picciotti, E.; Marzano, F.S. Evaluation of a new polarimetric algorithm for rain-path attenuation correction of X-band radar observations against disdrometer. *IEEE Trans. Geosci. Remote Sens.* **2014**, *52*, 1369–1380. [CrossRef]
16. Mishchenko, M.I.; Travis, L.D.; Mackowski, D.W. T-matrix computations of light scattering by nonspherical particles: A review. *J. Quant. Spectrosc. Radiat. Transf.* **1996**, *55*, 535–575. [CrossRef]

17. Ryzhkov, A.V.; Giangrande, S.E.; Melnikov, V.M.; Schuur, T.J. Calibration issues of dual-polarization radar measurements. *J. Atmos. Ocean. Technol.* **2005**, *22*, 1138–1155. [CrossRef]
18. Trabal, J.M.; Gorgucci, E.; Chandrasekar, V.; McLaughlin, D.J. Evaluation of the self-consistency principle for calibration of the CASA radar network using properties of the observed precipitation medium. *IEEE Trans. Geosci. Remote Sens.* **2014**, *52*, 149–162. [CrossRef]
19. Bringi, V.N.; Chandrasekar, V. *Polarimetric Doppler Weather Radar: Principles and Applications*; Cambridge University Press: Cambridge, UK, 2001; ISBN 1139429469.
20. Scarchilli, G.; Gorgucci, V.; Chandrasekar, V.; Dobaie, A. Self-consistency of polarization diversity measurement of rainfall. *IEEE Trans. Geosci. Remote Sens.* **1996**, *34*, 22–26. [CrossRef]
21. Andsager, K.; Beard, K.V.; Laird, N.F. Laboratory measurements of axis ratios for large raindrops. *J. Atmos. Sci.* **1999**, *56*, 2673–2683. [CrossRef]
22. Beard, K.V.; Chuang, C. A new model for the equilibrium shape of raindrops. *J. Atmos. Sci.* **1987**, *44*, 1509–1524. [CrossRef]
23. Barber, P.; Yeh, C. Scattering of electromagnetic waves by arbitrarily shaped dielectric bodies. *Appl. Opt.* **1975**, *14*, 2864–2872. [CrossRef] [PubMed]
24. Beard, K.; Jameson, A. Raindrop canting. *J. Atmos. Sci.* **1983**, *40*, 448–454. [CrossRef]
25. Bringi, V.; Chandrasekar, V.; Balakrishnan, N.; Zrnic, D. An examination of propagation effects in rainfall on radar measurements at microwave frequencies. *J. Atmos. Ocean. Technol.* **1990**, *7*, 829–840. [CrossRef]
26. Jameson, A. Polarization radar measurements in rain at 5 and 9 GHz. *J. Appl. Meteorol.* **1991**, *30*, 1500–1513. [CrossRef]
27. Brandes, E.A.; Ikeda, K. Freezing-level estimation with polarimetric radar. *J. Appl. Meteorol.* **2004**, *43*, 1541–1553. [CrossRef]
28. Shakti, P.C.; Maki, M.; Shimizu, S.; Maesaka, T.; Kim, D.S.; Lee, D.I.; Iida, H. Correction of Reflectivity in the Presence of Partial Beam Blockage over a Mountainous Region Using X-Band Dual Polarization Radar. *J. Hydrometeorol.* **2013**, *14*, 744–764.